ACS APPLIED MATERIALS & INTERFACES

Research Article

www.acsami.org

Surfactant-Assisted Synthesis of Fe_2O_3 Nanoparticles and F-Doped Carbon Modification toward an Improved $Fe_3O_4@CF_x/LiNi_{0.5}Mn_{1.5}O_4$ Battery

Hai Ming,[†,‡,§] Jun Ming,*[,‡] Seung-Min Oh,[‡] Shu Tian,[†] Qun Zhou,[†] Hui Huang,[§] Yang-Kook Sun,*[,‡] and Junwei Zheng*[,†]

[†]College of Chemistry, Chemical Engineering and Materials Science, Soochow University, Suzhou, Jiangsu 215123, People's Republic of China

[‡]Department of Energy Engineering, Hanyang University, Seoul 133-791, Republic of Korea

[§]Institute of Functional Nano & Soft Materials (FUNSOM) and Collaborative Innovation Center of Suzhou Nano Science and Technology, Soochow University, Suzhou, Jiangsu 215123, People's Republic of China

Supporting Information

ABSTRACT: A simple surfactant-assisted reflux method was used in this study for the synthesis of cocklebur-shaped Fe_2O_3 nanoparticles (NPs). With this strategy, a series of nanostructured Fe_2O_3 NPs with a size distribution ranging from 20 to 120 nm and a tunable surface area were readily controlled by varying reflux temperature and the type of surfactant. Surfactants such as cetyltrimethylammonium bromide (CTAB), polyvinylpyrrolidone (PVP), poly(ethylene glycol)-*block*-poly(propylene glycol)-*block*-poly(ethylene glycol) (F127) and sodium dodecyl benzenesulfonate (SDBS) were used to achieve large-scale synthesis of uniform Fe_2O_3 NPs with a relatively low cost. A new composite of $Fe_3O_4@CF_x$ was prepared by coating the primary Fe_2O_3 NPs with a layer of F-doped carbon (CF_x) with a one-step carbonization process. The $Fe_3O_4@CF_x$ composite was utilized as the anode in a lithium ion battery and exhibited a high reversible capacity of 900 mAh g^{-1} at a current density of 100 mA g^{-1} over 100 cycles with 95% capacity retention. In addition, a new $Fe_3O_4@CF_x/LiNi_{0.5}Mn_{1.5}O_4$ battery with a high energy density of 371 Wh kg^{-1} (vs cathode) was successfully assembled, and more than 300 cycles were easily completed with 66.8% capacity retention at 100 mA g^{-1}. Even cycled at the high temperature of 45 °C, this full cell also exhibited a relatively high capacity of 91.6 mAh g^{-1} (vs cathode) at 100 mA g^{-1} and retained 54.6% of its reversible capacity over 50 cycles. Introducing CF_x chemicals to modify metal oxide anodes and/or any other cathode is of great interest for advanced energy storage and conversion devices.

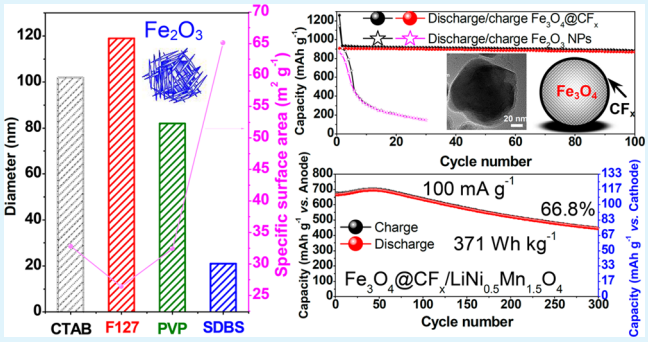

KEYWORDS: *nanoparticles, oxides, carbon, electrochemical properties, batteries*

INTRODUCTION

Metal oxides have been investigated worldwide as a potential anode material in lithium ion batteries (LIBs) due to their higher theoretical specific capacity (>800 mAh g^{-1}) when compared to commercial graphite (~372 mAh g^{-1}). Moreover, the relatively high operating potential near 0.8 V (vs ~0.2 V of graphite) could effectively avoid the safety problem of lithium deposition on the anode during fast charge.[1−3] To date, numerous studies regarding metal oxides with different morphologies (e.g., solid, hollow, or core−shell particles and wires, or a hierarchical structure) and/or chemical compositions (e.g., SiO_x,[4−6] SnO_2,[7] Fe_2O_3,[8,9] Fe_3O_4,[10−12] Co_3O_4,[13,14] NiO,[15] CuO,[16,17] Co_3O_4/TiO_2,[18] $SnO_2@TiO_2$,[19] $SnO_2@Fe_2O_3$[20]) have been published describing a series of synthetic approaches including a solvent-thermal method, precipitation, direct calcination, chemical vapor deposition, supercritical fluid deposition and so on. Indeed, these kinds of metal oxides exhibit a high capacity and stability in LIBs, particularly when combined with carbon modification, coating, supporting or encapsulation.

However, as far as we know, these methods and the amount of products are still limited on an experimental scale. Consideration of possible large-scale, industrial production for practical applications is warranted.[21] Therefore, we developed a simple surfactant-assisted reflux method to synthesize Fe_2O_3 nanoparticles (NPs) in large quantities. A series of nanostructured Fe_2O_3 NPs with size distribution ranging from 20 to 120 nm were readily prepared by varying temperature and the

Received: June 26, 2014
Accepted: August 20, 2014
Published: August 20, 2014

type of surfactant. A new Fe_3O_4@CF_x composite was introduced by coating the primary size-controlled Fe_2O_3 NPs with a layer of CF_x through carbonization of polyvinylidene fluoride (PVDF) rather than a traditional carbon coating process.

Recently, the elemental doping of B, N, F or P into carbon structures is of great interest because of their excellent performance in the fields of catalysis, electrochemistry, energy and nano devices.[22] For example, as shown by first-principles calculations and previous experimental results, a coating layer of N-doped carbon (CN_x) can significantly improve interfacial stability and electric conductivity,[23] thereby enhancing the performance of the metal oxides FeO_x and CoO_x in LIBs.[24] In addition, N, B and P multidoped carbon, F-doped carbon (CB-F) and P-doped porous carbon could be used as effective metal-free catalysts for oxygen reduction.[25,26] Few studies have focused on coating a conductive layer of F-doped carbon (CF_x) on materials such as electrodes due to the difficult preparation of CF_x with high purity on a large scale. To investigate the potential properties of this kind of material, we experimented with one method for PVDF carbonization to prepare CF_x that involved coating Fe_2O_3 NPs. It is well-known that PVDF is an excellent binder that can facilely surround metal oxides or other electrode materials and uniform coating of CF_x after carbonization.[27] Moreover, the use of PVDF could enable clean, large-scale production of CF_x. Therefore, we prepared a Fe_3O_4@CF_x composite and evaluated its electrochemical properties in a LIB. It delivered a high capacity of 900 mAh g^{-1} with good cycling ability over 100 cycles and capacity retention of 95%. Cyclic voltammetry (CV) and impedance analyses of the CF_x modified electrode proved that CF_x can enhance the electrode conductivity and also ensures rapid Li^+ diffusion with lower interfacial resistance. This new methodology could be readily extended to modify other anode or cathode materials for advanced energy storage and conversion devices.

Although these metal oxides have been widely investigated as anodes in lithium ion batteries, most studies only focused on their properties in half cells that used lithium metal as the counter electrode, rather than in a certain type of cathode materials. Several promising studies tried to assemble full batteries using Fe_3O_4-graphene/$LiNi_{1/3}Co_{1/3}Mn_{1/3}O_2$,[28] Fe_2O_3/$LiFePO_4$,[29] B-TiO_2/$LiNi_{0.5}Mn_{1.5}O_4$,[30] CuO/$LiNi_{0.5}Mn_{1.5}O_4$,[31] MnO/$LiNi_{0.5}Mn_{1.5}O_4$[32] and PC-Fe_3O_4/$Li[Ni_{0.59}Mn_{0.16}Co_{0.25}]O_2$.[33] It was confirmed that the electrode properties could be evaluated more accurately in this way, and also it provided a more practical method for facilitating development of the metal oxide toward commercialization. Considering the low cost, rich abundance, suitable voltage around 0.8 V and environmentally friendly nature of ferric oxide combined with the facile large-scale synthesis, high capacity and stability of Fe_3O_4@CF_x, we attempted to assemble a new Fe_3O_4@CF_x/$LiNi_{0.5}Mn_{1.5}O_4$ battery. We selected spinel phase $LiNi_{0.5}Mn_{1.5}O_4$ due to the fact that it is commercially available and has a high voltage platform around 4.7 V, which is suitable for achieving a high work voltage and cellular energy density. Preliminary results showed that the cell could deliver a high reversible capacity of 664 mAh g^{-1} (vs anode of Fe_3O_4@CF_x) at a current density of 100 mA g^{-1} with an operating potential of approximately 3.2 V. The cycling ability greater than 300 cycles with a capacity retention of 66.8% at a current density of 100 mA g^{-1} was largely improved compared to the previous results for Fe_3O_4 or Fe_2O_3 based anode in a full cell,[25,26] particularly at a high energy density of 371 Wh kg^{-1}.

EXPERIMENTAL SECTION

Materials Synthesis. In a typical synthesis reaction, 200 mL of $NH_3{\cdot}H_2O$ was introduced into 3000 mL of aqueous CTAB (30.0 g) and $Fe(NO_3)_3{\cdot}9H_2O$ (160 g) at 25 °C under vigorous stirring. Then, the as-prepared solution was stirred vigorously at 95 °C for 12 h, and calcined at 823 K for 4 h (the heating rate is 2 °C min^{-1}), which yielded red Fe_2O_3−CTAB (95) NPs, where CTAB and 95 refer to the kind of surfactant and reflux temperature. Furthermore, Fe_2O_3−CTAB(75) and Fe_2O_3−CTAB(120) were prepared by varying the temperature of the solution (75 and 120 °C). The Fe_2O_3−F127 (95), Fe_2O_3−PVP (95) and Fe_2O_3−SDBS (95) NPs were prepared by exchanging the surfactants (F127, PVP and SDBS) used. To prepare the Fe_3O_4@CF_x, 10 g of the Fe_2O_3−CTAB-95 powder and 2.5 g of PVDF were added to 50 mL of NMP, The mixture was dried in an oven (120 °C) for 10 h, and then calcined in a tube furnace at 600 °C (2−5 °C min^{-1}) for 1 h, which yielded the Fe_3O_4@CF_x product. The normal carbon coated Fe_3O_4@C particles were prepared with using the poly ethylene (PE) and sucrose (SC) as the carbon precursors under the same process, respectively. The naked Fe_3O_4 particles were prepared based on the procedures as reported previously.[12]

Electrode Preparation. The cell tests were carried out using a 2032-type coin-shaped cell, in which a metallic lithium film, microporous polypropylene film (Celgard2400) and 1.0 mol L^{-1} $LiPF_6$ in a mixture of dimethyl carbonate (DEC) and ethylene carbonate (EC) (v/v, 1/1) were used as the counter, separator and electrolyte, respectively. The Fe_3O_4@CF_x-based electrode was prepared by mixing a slurry of active material containing carbon black (Super P), and PVDF with a weight ratio of 8:1:1 in NMP. Then the slurry was coated onto the copper foil with an automatic film applicator. The film was dried in a vacuum oven at 120 °C for 12 h and cut it into circular sheets (o.d. is 14 mm), which were further dried in a vacuum oven at 120 °C for 12 h. The mass density of Fe_3O_4@CF_x was about 1.5 mg cm^{-2}. The cells were assembled in a glovebox filled with pure argon, in which the moisture and oxygen were strictly controlled to be less than 0.1 ppm. The cells had a configuration of Li metal (−) | separator | electrode (+) in the liquid electrolyte. The $LiNi_{0.5}Mn_{1.5}O_4$ electrodes were prepared using the same process as that used for the Fe_3O_4@CF_x electrode ($LiNi_{0.5}Mn_{1.5}O_4$:Super P:KS6:PVDF = 8.5:0.5:0.5:0.5, weight ratio), except aluminum foil was used instead of Cu foil. The mass density of $LiNi_{0.5}Mn_{1.5}O_4$ was about 9 mg cm^{-2}. The mass ratio of the cathode and anode was controlled to be 6 since the Fe_3O_4@CF_x electrode had been lithiated before assembling the full cell.[12] Galvanostatic charge and discharge experiments full cells were conducted using TOCAST 3100 at several different current densities between cutoff potentials of 2.0 to 4.6 V.

Characterization. The crystal information was characterized by the X-ray powder diffraction (XRD) using a X'Pert-ProMPD (Holand) D/max-γA X-ray diffractometer with Cu Kα radiation (λ = 0.154 178 nm). Scanning electron microscopy (SEM) was conducted on a FEI-quanta 200F scanning electron microscope with acceleration voltage of 30 kV. The distribution of Fe_2O_3 and Fe_3O_4@CF_x samples were characterized by the transmission electron micrograph (TEM) with using the FEI-Tecnai F20 (200 kV) transmission electron microscope. Nitrogen adsorption−desorption isotherms were obtained using the ASAP2050 instrument (Micromeritics Industrument Corp.) surface area and porosity Analyzer at −196 °C. The specific surface area was calculated by the Brunauer−Emmett−Teller (BET) method. Thermogravimetric analysis (TGA, NETZSCH, TG-209-F3) was carried out under a flow of air with a temperature ramp of 5 °C min^{-1}. All the electrochemical measurements were tested and recorded automatically by the TOCAST 3100 instrument at the temperature of 30 °C. Cyclic voltammetry (CV) within the voltages of 0.01−3.0 V and impedance analysis in the frequency ranging from 100 kHz and 10 mHz were both performed using the VMP-3 instrument.

RESULTS AND DISCUSSION

In a typical round of synthesis, 200 mL $NH_3{\cdot}H_2O$ was introduced into a 3000 mL aqueous solution of CTAB (30.0 g) and $Fe(NO_3)_3{\cdot}9H_2O$ (160 g) at 25 °C with vigorous stirring,

subsequently increasing the temperature to 95 °C for 12 h under reflux. The solution was then filtered in order to extract the intermediates, and the resulting dried powder was then calcined at 600 °C for 4 h (the heating rate is 2 °C min^{-1}). This step yielded Fe_2O_3–CTAB-95, a red product (CTAB and 95 correspond to the kind of surfactant and the reaction temperature used in the system, respectively). In the same way, Fe_2O_3–CTAB-75 and Fe_2O_3–CTAB-120 were also prepared by varying the reaction temperature to 75 and 120 °C, respectively. The XRD patterns (Figure 1a–c) confirmed

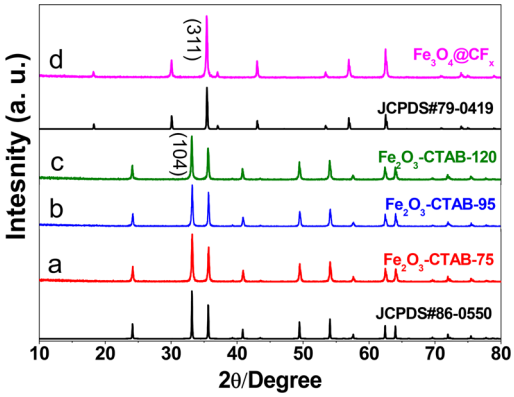

Figure 1. XRD patterns of Fe_2O_3 NPs prepared with the assistance of CTAB at different synthesis temperatures, Fe_3O_4@CF_x, and the standard patterns of Fe_2O_3 and Fe_3O_4.

that the crystalline structure of these three powders (Fe_2O_3–CTAB-75, 95, 120) was ascribed to the presence of normal Fe_2O_3 (JCPDS Card No. 86-550), the amount of which was mainly determined by the postcalcination temperature. Low-magnification SEM images indicated that these Fe_2O_3–CTAB NPs were produced on a large scale with a uniform size distribution and a controlled morphology (Figure S1, Supporting Information). As shown in Figure 2, the Fe_2O_3–CTAB NPs underwent an evolution from a mixture of integral and fragmented Fe_2O_3 nanoparticles (Fe_2O_3–CTAB-75), to a uniform cocklebur-like appearance (Fe_2O_3–CTAB-95), and finally to smooth nanospheres (Fe_2O_3–CTAB-120), confirming that the reaction temperature played an important role in intermediate self-assembly. The morphology of the Fe_2O_3–CTAB-75 powder consisted primarily of nanoparticles with a diameter of 100 nm and numerous distributed primary nanosheets with a diameter less than or approximately equal to 50 nm (Figure 2d). The structure of the Fe_2O_3–CTAB-95 powder consisted of two morphologies: the major inner NPs with diameters around 100 nm, and the other attached to plentiful smaller nanosheets, giving a cocklebur-like appearance. This difference in morphology illustrates that a high temperature is suitable for facilitating the self-assembly of primary nanosheets to enable growth of integral particles. This conclusion was further confirmed by the 120 nm, uniform and smooth spheres in the Fe_2O_3–CTAB-120 powder. Note that the obtained Fe_2O_3 nanoparticles consisted of numerous nanocrystals with a lattice fringe spacing of 0.27 nm, which corresponds to the spacing of the (104) planes of Fe_2O_3. The N_2 adsorption–desorption isotherms of the Fe_2O_3–CTAB (75, 95, 120) curves show a well-defined adsorption step and are the typical type IV (Figure S2, Supporting Information).[34,35] Owing to their different structures, the BET specific surface areas and pore volumes of the Fe_2O_3–CTAB-75, 95, and 120 samples were 20.1, 32.8, 11.8 m^2 g^{-1} and 0.21, 0.27, 0.18 cm^3 g^{-1}, respectively, with the majority of pores approximately 30, 130 and 25 nm, respectively. The large pore size resulted primarily from the accumulation of Fe_2O_3 nanoparticles, especially in the Fe_2O_3–CTAB-120 sample.

We also experimented with using different surfactants at a constant synthesis temperature to prepare Fe_2O_3–F127–95, Fe_2O_3–PVP-95 and Fe_2O_3–SDBS-95 NPs, which had different sizes and surface architecture (Figure 3a–c). All three of these

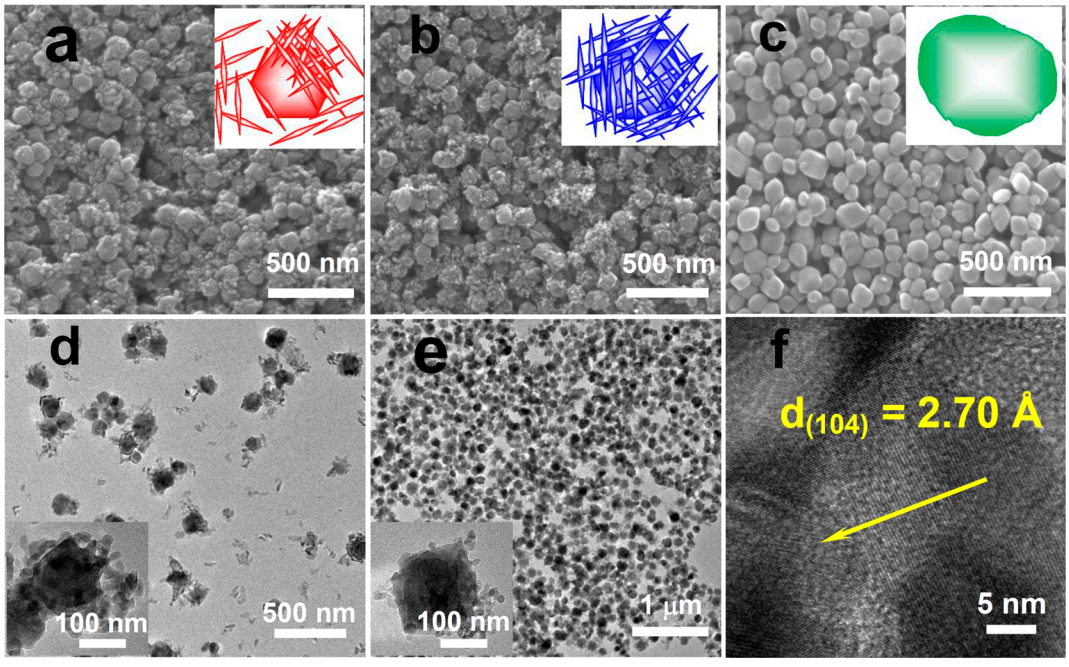

Figure 2. SEM, TEM and HRTEM of Fe_2O_3 NPs prepared in the assistance of CTAB under different temperatures of (a, d) 75, (b, e) 95 and (c, f) 120 °C. Each inset is the detail structure of Fe_2O_3 NPs, respectively.

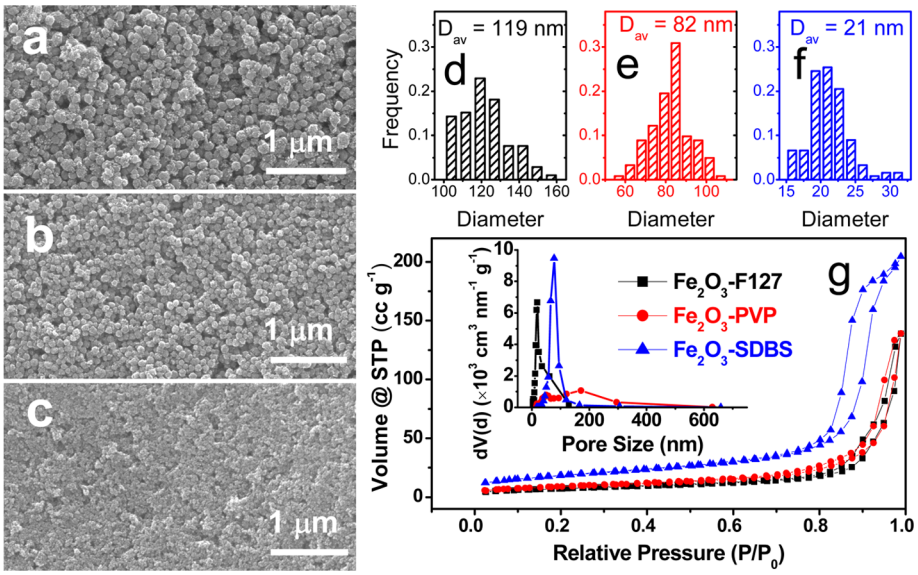

Figure 3. SEM images and the particle size distribution of Fe_2O_3 NPs synthesized using (a, d) F127, (b, e) PVP and (c, f) SDBS. (g) Corresponding nitrogen adsorption−desorption isotherms with the insets showing their BJH pore size distribution.

samples had a normal α-Fe_2O_3 crystalline structure (Figure S3, Supporting Information). All three powders consisted of spherical NPs with average sizes of about 119, 82 and 21 nm, respectively (Figure 3d−f). Comparative images show that the SDBS was good for preparing small Fe_2O_3 NPs, whereas the PVP was preferable for maintaining the uniformity of the Fe_2O_3 particles. The specific surface areas and pore volumes (Figure 3g) of the Fe_2O_3−F127−95, Fe_2O_3−PVP-95 and Fe_2O_3−SDBS-95 samples were 26.4, 32.4, 65.1 $m^2\ g^{-1}$ and 0.22, 0.22 and 0.33 $cm^3\ g^{-1}$, respectively, with pore sizes of 18, 171 and 76 nm, respectively. It is evident that Fe_2O_3 nanoparticles with different morphologies, size distributions and surface areas can be readily prepared on a large scale to be used in applications such as catalysis, sensors, electrochemistry and energy.

Fe_3O_4@CF_x NPs were prepared using a typical evaporation-induced self-assembly (EISA) method, in which PVDF and NMP were used as the precursor and solvent, respectively, in order to coat the Fe_2O_3−CTAB-95 with a layer of CF_x after drying and carbonization. Due to the reducing ability of PVDF in argon at elevated temperature, the Fe_2O_3 was deoxidized during the carbonization of PVDF (Fe_2O_3 + $(C_2H_2F_2)_n$ → Fe_3O_4@CF_x + CO/CO_2 + H_2O + C_xH_y). The XRD patterns of the Fe_3O_4@CF_x NPs revealed that the sample was consistent with the magnetite structure of Fe_3O_4 (JCPDS card No. 79-419) (Figure 1d). No diffraction peaks indicating possible impurities (e.g., FeC_x, Fe_2O_3) were detected. SEM images (Figure 4a) showed that the Fe_3O_4@CF_x NPs were interconnected and the surface of the materials was rougher than that of pristine Fe_2O_3−CTAB-95 (Figure 1c). The EDX spectrum (Figure 4b) revealed that the mass percentages of Fe, O, C and F in the Fe_3O_4@CF_x NPs were about 70.29%, 17.52%, 10.30% and 1.89%, respectively, which confirmed that about 12.19% CF_x was present in the composite, and the EDX elemental mapping of F and C in Fe_3O_4@CF_x NPs (Figure 4c−f) confirmed that the C and F elements are in a homogeneous distribution. Meanwhile, the characteristics and structure of CF_x were confirmed by TEM. As shown in Figures 5a−c, the Fe_3O_4 particles were indeed completely coated by one amorphous layer with a thickness of 1−3 nm (marked by the red arrow). The well-resolved lattice fringes with an interplane distance of

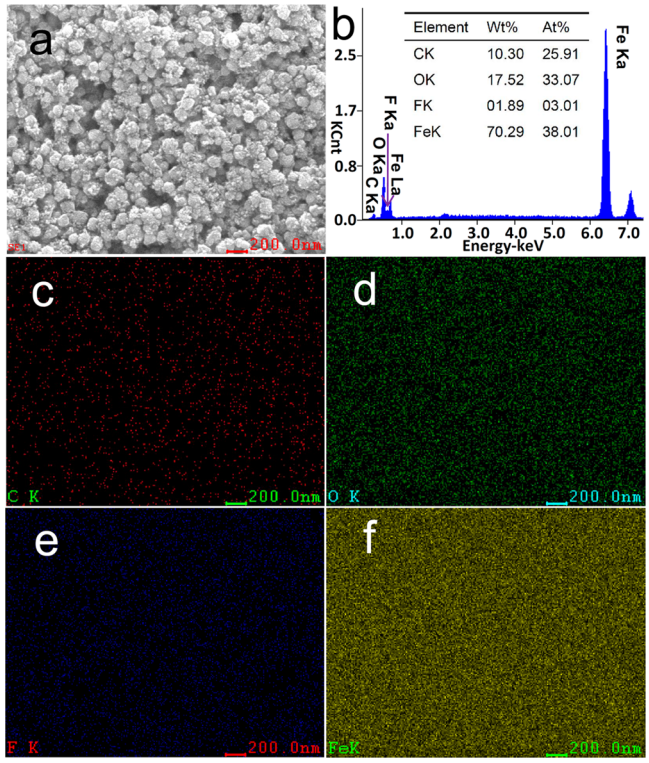

Figure 4. (a) SEM image, (b) EDX spectrum and (c−f) elemental mapping of Fe_3O_4@CF_x NPs.

0.253 nm comes from the (311) plane of Fe_3O_4, and a clear interfacial region of CF_x and Fe_3O_4 could be observed. The formation of CF_x resulted from the carbonization of PVDF, which contains 59 wt % of F.[36] The weight loss of 11.5% noted in the TGA curve (Figure 5d) corresponded to the removal of elemental C and F, which is consistent with the EDX analysis results (12.19%, a little bit higher than that of TGA date because the CF_x is mainly on the surface of Fe_3O_4). The porosity of Fe_3O_4@CF_x NPs was characterized by the N_2 adsorption−desorption isotherm and Barrett−Joyner−Halenda

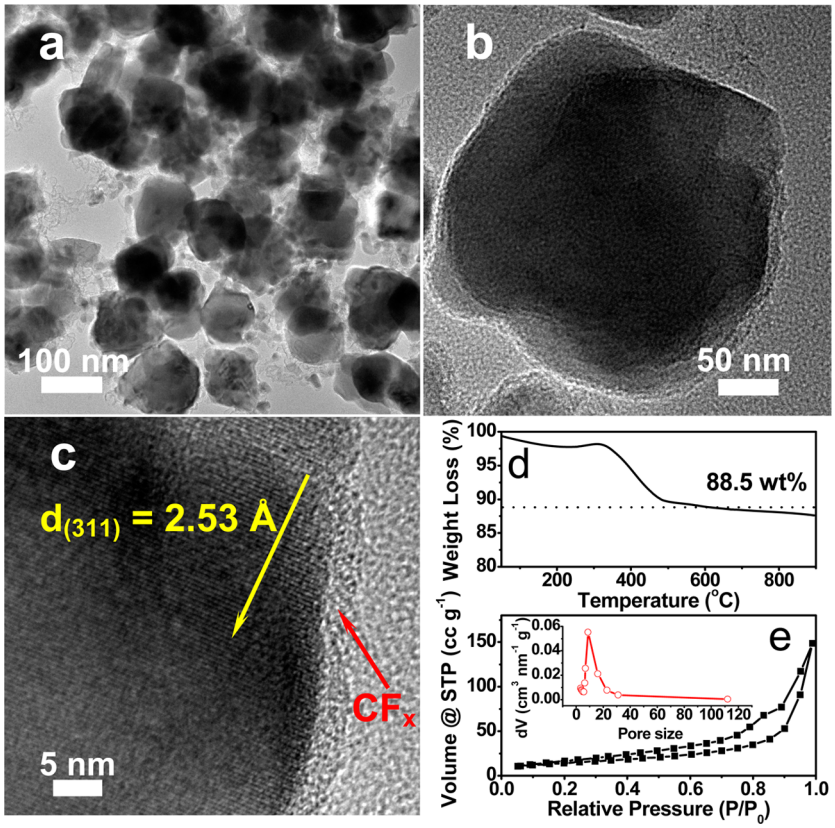

Figure 5. (a, b) TEM and (c) HRTEM images, and (d) TGA and (e) BET analyses of Fe_3O_4@CF_x particles.

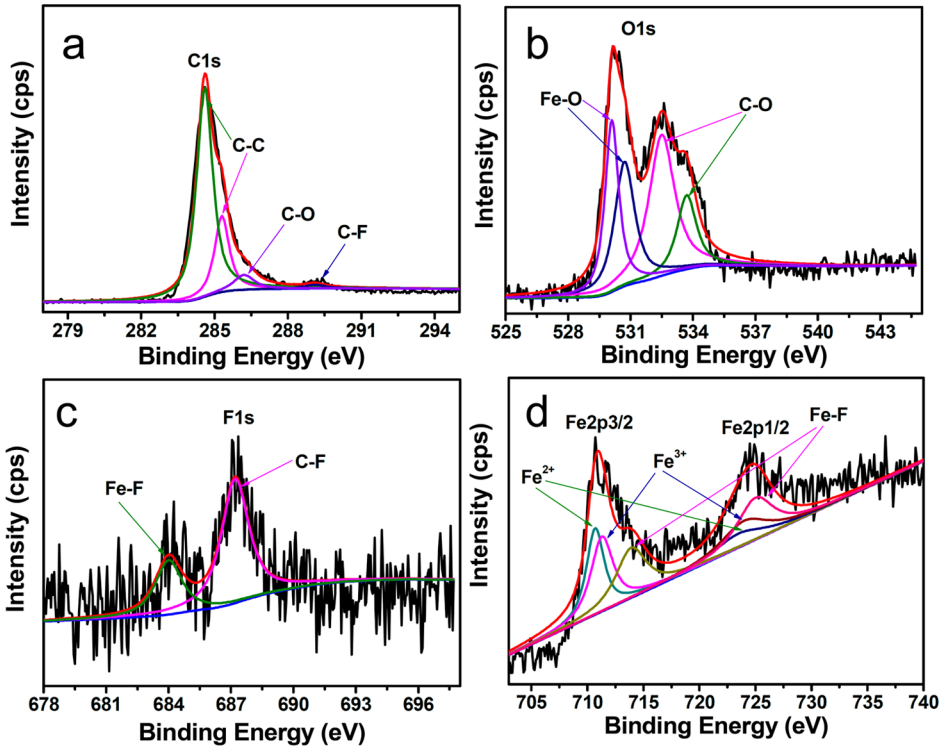

Figure 6. High-resolution XPS spectra of the (a) C 1s, (b) O 1s, (c) F 1s and (d) Fe $2p_{3/2}$ and Fe $2p_{1/2}$ regions of the as-prepared Fe_3O_4@CF_x NPs.

(BJH) plots (Figure 5e), which showed a typical type-IV isotherm and a narrow size distribution around 10 nm. The BET specific surface area and pore volume of the Fe_3O_4@CF NPs were 50.8 m^2 g^{-1} and 0.23 cm^3 g^{-1}, respectively. The increase in surface area from 32.8 to 50.8 m^2 g^{-1} was consistent with the rougher surface of the Fe_3O_4@CF_x particles.

The chemical compositions of the Fe_3O_4@CF_x NPs, particularly with regard to C and F, were further confirmed

dx.doi.org/10.1021/am504144d | ACS Appl. Mater. Interfaces 2014, 6, 15499−15509

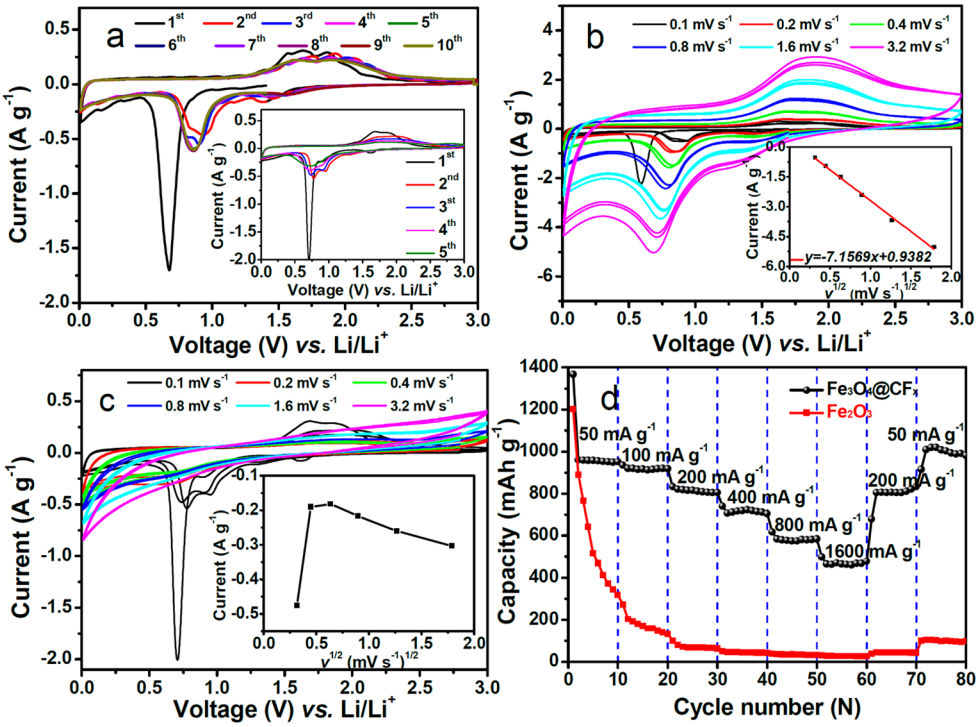

Figure 7. Cyclic voltammograms (CV) of (a) Fe_3O_4@CF_x with the inset showing the (a) Fe_2O_3 NP electrode at different scan rates at 0.1 mV s^{-1}. (b) Fe_3O_4@CF_x and (c) Fe_2O_3 NP electrode ranging from 0.1 to 3.2 mV s^{-1}. The insets in panels b and c show the relationship between the peak current and the square root of the scan rate. (d) Comparative rate capability of the Fe_3O_4@CF_x and (c) Fe_2O_3 NP electrodes.

by X-ray photoelectron spectroscopy (XPS). The C 1s, O 1s, F 1s and Fe 2p and Fe 3p peaks are an accurate representation of the elemental composition of the composite. Figure 6a shows the C 1s, in which the four prominent fitting peaks around 284.6 (285.3), 286.2 and 289.1 eV correspond to the C−C, C−O and C−F chemical bands, respectively.[37] The fitting peaks of O 1s at 532.5 and 533.6 eV indicate that O atoms combined with C atoms (C−O−Fe),[38] and peaks corresponding to Fe−O chemical bonds at 530.7 and 530.1 eV were also observed (Figure 6b).[39] Note that the fitting peaks (Figure 6c) of F 1s at 687.2 and 684 eV indicate that F atoms not only combined with C atoms[40] but were also doped in the Fe_3O_4 NPs.[41] In the XPS spectrum of Fe $2p_{3/2}$ and $2p_{1/2}$ (Figure 6d), the dominating peaks at 711.3 and 724 eV belong to Fe^{3+}, and the other Fe^{2+} satellite peaks at 710.7 and 723.5 eV indicate the reduction of Fe^{3+} to Fe^{2+} in the product with the carbonization of PVDF.[42] Interestingly, we identified two peaks located at 713.9 and 725 eV, which corresponds to the Fe−F chemical bonds due to traces amount of presence FeF_3.[43,44] In brief, these results confirm that the Fe_3O_4 NPs were indeed coated with a layer of F-doped carbon, and also a small amount of amorphous FeF_3 formed at the interface of the Fe_3O_4 and CF_x.

The electrochemical performance of Fe_3O_4@CF_x NPs in LIBs was first investigated in a half-cell test. A good cycling performance of Fe_3O_4@CF_x electrode was preliminarily observed in the cyclic voltammograms (CV) for the initial ten cycles, during which the intensity of the cathodic peaks (i.e., reduction of Fe^{3+}/Fe^{2+} to Fe^0) remained around 0.8 V, except during first cycle, which corresponded to the formation of a solid-electrolyte interphase (SEI). This finding was further confirmed by broad anodic peaks around 1.69 V (i.e., the reversible oxidation of Fe^0 to Fe^{2+}/Fe^{3+}), the intensity of which also remained the same.[45] In contrast, the electrode fabricated using primary Fe_2O_3 NPs exhibited a serious decrease in the intensities of the cathodic and anodic peaks during cycling. In order to understand the solid phase diffusion-controlled or surface-confined charge-transfer processes of the as-prepared sample, CV experiments were conducted under different scan rates (Figure 7), each rate cycled three times. Normally, the peak intensity will increase with increasing scan rate and the cathodic peaks shift to a lower potential while the anodic peaks shift to a higher potential (Figure 7b,c), indicating an increase in electrochemical polarization. The linear dependence of the peak current (i_p) on the square root of the scan rate ($v^{1/2}$) is indicative of a diffusion-limited reaction in the cathodic process for the different samples. This relationship is known as the typical Randles−Sevcik relation, expressed as follows: $i_p = 0.4463n^{3/2}F^{3/2}C_{Li}SR^{-1/2}T^{-1/2}D_{Li}{}^{1/2}v^{1/2}$, where n (charge transfer number), F (Faraday constant), C_{Li} (Li-ion concentration), S (surface area of the electrode), R (gas constant) and T (absolute temperature, K) are all constant.[46] The variable D_{Li} is the diffusion coefficient. The larger it is, the faster the lithium ions diffuse into the electrodes. Clearly, the D_{Li} of the Fe_3O_4@CF_x NP samples was better than that of the Fe_2O_3 NP samples, indicating that the Fe_3O_4@CF_x NP electrodes possess a rapid lithium ion diffusibility. This finding was further confirmed by the rate performance of the cell. As shown in Figure 7d, the Fe_3O_4@CF_x electrode delivered discharge capacities of 951, 918, 804, 704, 584 and 477 mAh g^{-1} at current densities of 50, 100, 200, 400, 800 and 1600 mA g^{-1}, respectively, and ultimately recovered to 832 mAh g^{-1} at 200 mA g^{-1} and 981 mAh g^{-1} at 50 mA g^{-1} successively. The results were much better than those for the electrode composed of Fe_2O_3 NPs (Figure 7d).

To have a better understanding of the conductivity and lithium ion diffusion ability of the pure Fe_2O_3 and Fe_3O_4@CF_x NP, the EIS of the electrode was further measured. The fresh cells with the electrode loading of 2.31 mg were tested in the

dx.doi.org/10.1021/am504144d | ACS Appl. Mater. Interfaces 2014, 6, 15499−15509

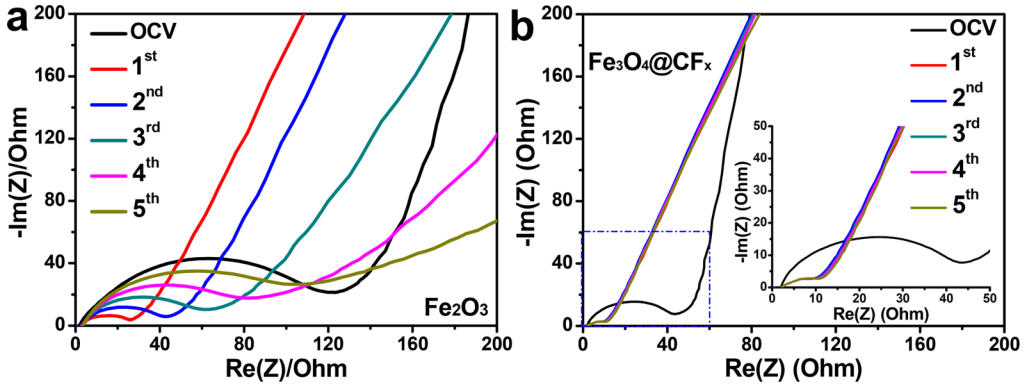

Figure 8. Nyquist plots of (a) pure Fe_2O_3 and (b) Fe_3O_4@CF_x electrodes from the OCV to the fifth cycles. Both cells are cycled at the current density of 100 mA g^{-1}.

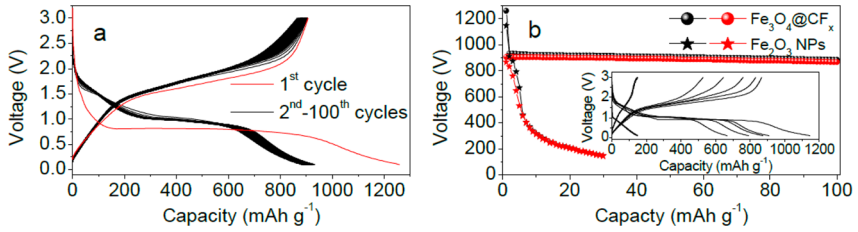

Figure 9. (a) Charge−discharge profiles of the Fe_3O_4@CF_x NP electrode, (b) comparative cycling performances of the Fe_2O_3 and Fe_3O_4@CF_x NP electrodes at a current density of 100 mA g^{-1}. The inset shows the corresponding voltage profiles of the Fe_2O_3 electrode.

full charge state and cycled at the current density of 100 mA g^{-1}. Figure 8 shows the Nyquist plots from the OCV (open circuit voltage) to the initial five cycles. Clearly, the Fe_3O_4@CF_x NP electrode exhibits much lower resistance, higher stability and lithium ion diffusion ability than that of the pure Fe_2O_3 NP electrode, as evidenced by the diameter of the semicircle at the high-frequency region and the steep sloping line at the low-frequency region in the EIS patterns.[47] Due to the CF_x layer's high electron and lithium ion transferring ability, as well as its protection of the metal oxide, the Fe_3O_4@CF_x composite demonstrated an average capacity of 900 mAh g^{-1} at a current density of 100 mA g^{-1} and an excellent cycling ability over 100 cycles (capacity retention, 95%), as shown in Figure 9a,b. The serious decay of the Fe_2O_3 NP electrode further confirmed that the CF_x layer maintained the good performance of the electrode materials. The performance of the Fe_3O_4@CF_x composite was largely improved compared to plain Fe_3O_4 NPs (~500 mAh g^{-1}),[48] Fe_3O_4@carbon (~600 mAh g^{-1}),[49] Fe_3O_4@graphene (~700 mAh g^{-1})[50] and Fe_3O_4@CN_x (~810 mAh g^{-1}).[51]

Besides, we further confirmed the difference of unique CF_x from the normal carbon. For example, two other kinds of carbon coated Fe_3O_4 particles such as Fe_3O_4@-C-PE and Fe_3O_4@C-SC were prepared with using poly ethylene (PE) and sucrose (SC) as the carbon precursors instead of PVDF under the similar process, respectively. Clearly, the capacity and the stability of the Fe_3O_4@CF_x were higher and better than those of Fe_3O_4@C-PE and Fe_3O_4@C-SC (Figure S4, Supporting Information), and it was confirmed that the advantages of CF_x was better than normal carbon to improve the performance of Fe_3O_4 particles. And also, the performances of Fe_3O_4@CF_x were better than that of naked Fe_3O_4 particles without any carbon modification (Figure S4, Supporting Information).

Moreover, the size effect of Fe_2O_3 particles was investigated. The products of Fe_3O_4@CF_x-big and Fe_3O_4@CF_x-small were prepared with using the Fe_2O_3−F127 (big, 119 nm) and Fe_2O_3−SDBS (small, 21 nm) as precursors, respectively. Compare to the composite of Fe_3O_4@CF_x prepared from the cocklebur-shaped Fe_2O_3 nanoparticles (e.g., 102 nm), the Fe_3O_4@CF_x demonstrated the best performance (Figure S4, Supporting Information). It is reasonable, because a big size of Fe_2O_3−F127 particles can cause the difficulty in the coating and reduction process, and also the big size of product (e.g., Fe_3O_4@CF_x-big) could cause large volume variation and pulverization during the repeated charge−discharge. Together with the low rate of electronic transfer ability in the large particles, the Fe_3O_4@CF_x-big demonstrated a low stability compared to that of Fe_3O_4@CF_x. Oppositely, if the size of Fe_2O_3−SDBS particles are too small and also have a large surface area, a large amount of the F-based compounds (e.g., FeF_3, FeF_2) would form between the interface of the Fe_3O_4 and CF_x, and also numerous interface barriers will also increase the electronic transferability of Fe_3O_4@CF_x-small composite. As a result, the capacity of the Fe_3O_4@CF_x-small is low but with a high stability due to the endurable volume variation of small particles. Simply, in this work, the ocklebur-shaped Fe_2O_3−CTAB nanoparticles with the suitable size are the best precursors for getting the Fe_3O_4@CF_x composite with the best electrochemical performance.

We also investigated the performance of Fe_3O_4@CF_x in a full battery versus a high-voltage $LiNi_{0.5}Mn_{1.5}O_4$ cathode, which was prepared under the guidance of Sun et al.[52,53] The SEM and XRD results showed that the $LiNi_{0.5}Mn_{1.5}O_4$ cathode powder comprised spherical particles with a size around 5−10 μm (Figure 10a, inset of Figure 10b). As shown in Figure 10b, the $LiNi_{0.5}Mn_{1.5}O_4$ cathode delivered a capacity of 135 mA g^{-1} with a voltage of 4.7 V, and the Fe_3O_4@CF_x anode exhibited a capacity around 920 mA g^{-1} with a voltage of ~1.1 V at a current density of 100 mA g^{-1}. After the full cell was assembled, it had an open circuit potential of ~2.28 V, and typical charge−

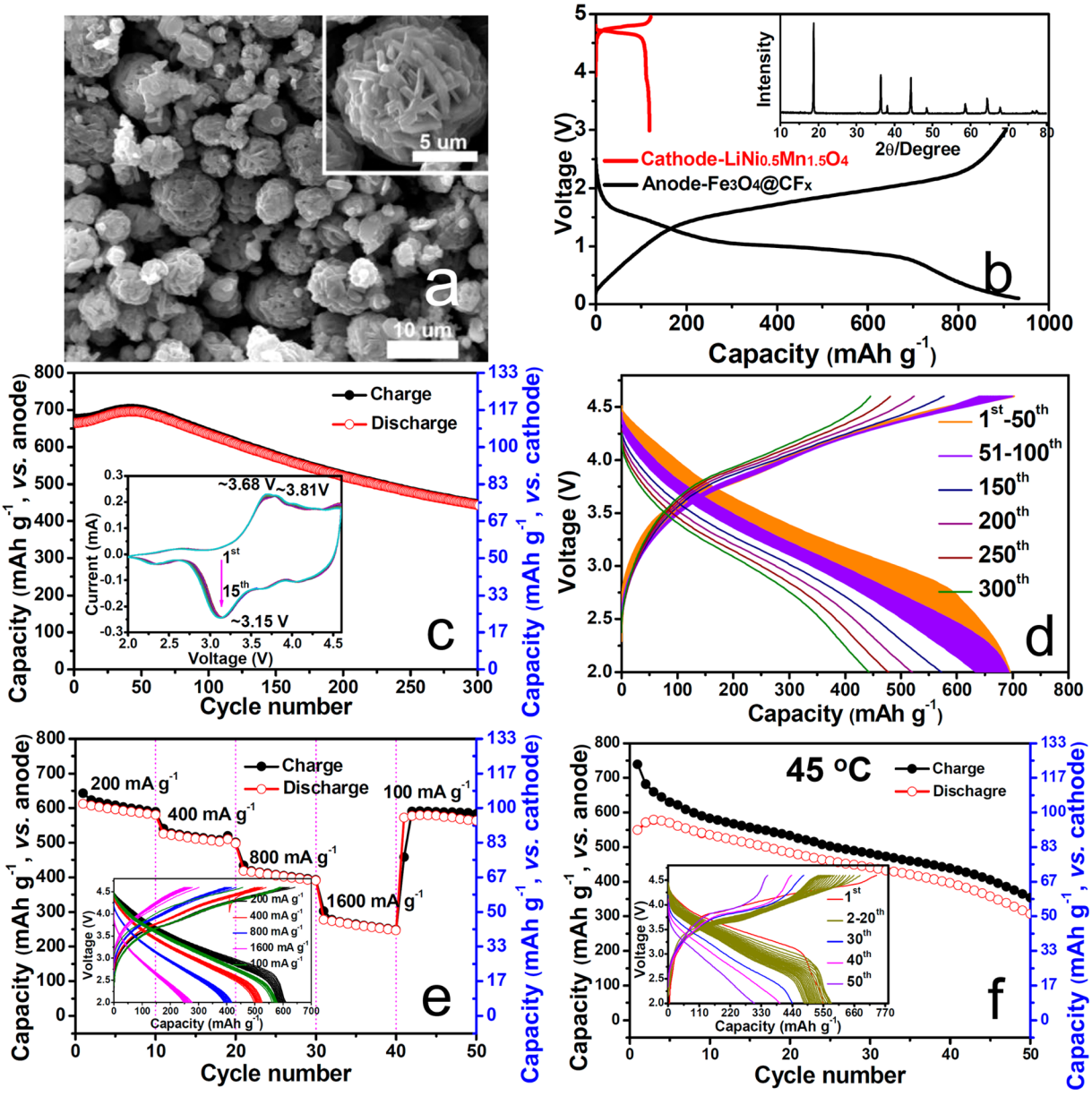

Figure 10. (a) SEM images of the $LiNi_{0.5}Mn_{1.5}O_4$ powders. (b) Comparative charge−discharge profiles of the Fe_3O_4@CF_x NP and $LiNi_{0.5}Mn_{1.5}O_4$ electrodes at a current density of 100 mA g^{-1}. The inset is the XRD pattern of $LiNi_{0.5}Mn_{1.5}O_4$. Full cell of the Fe_3O_4@CF_x/$LiNi_{0.5}Mn_{1.5}O_4$: (c) cycling performance and CV curves, (d) voltage profiles, (e) cycling performance and voltage profiles at the different current densities (200−1600 mA g^{-1}), (f) cycling performance and voltage profiles at the high temperature of 45 °C.

discharge curves cycled between 2.0 and 4.6 V at a current density of 100 mA g^{-1} from the 1st to the 300th cycles (Figure 10c,d). The cell had a high working voltage around 3.2 V and could cycle well beyond 300 cycles with a capacity retention of 66.8%. The reversible capacities of the cell were 664 mAh g^{-1} (vs anode) and 110.7 mAh g^{-1} (vs cathode) at a current density of 100 mA g^{-1} with an energy density of about 371 kWh kg^{-1} (i.e., the value was calculated by the integral of the discharge curve in the voltage-capacity profile, vs cathode). The CV curves (inset in Figure 10c) with well paired redox peaks and voltage profiles (Figure 10d) with long platform also confirmed the well paired of the anode and cathode in this full cell, implying a high reversibility. With varying the current density from 200, 400, 800 to 1600 mA g^{-1}, the cathode of $LiNi_{0.5}Mn_{1.5}O_4$ in this cell could still work well with capacities of 103, 83, 67 and 41 mAh g^{-1} (Figure 10e). Finally, the cell could recover back to 98 mAh g^{-1} (vs cathode) at the current density of 100 mA g^{-1}, demonstrating the good rate capability and stability of the electrode materials. Furthermore, a high capacity of about 91.6 mAh g^{-1} (vs cathode) was still obtained after further increasing the test temperature to 45 °C at the current density of 100 mA g^{-1}, and the capacity retention is 54.6% over 50 cycles. The energy density remained around 316 Wh kg^{-1} (Figure 10f, calculated from the discharge curve of the third cycle). Note that the capacity values of 664 mAh g^1 (30 °C) and 549.6 mAh g^{-1} (45 °C) were much higher that of commercial graphite in a full cell (about 240 mAh g^{-1}) at a similar current density. And the working potential was much higher than those of aqueous-based rechargeable battery systems such as lead-acid, Ni−Cd, Ni−MH and lithium−sulfur batteries, this full cell was also superior with an accepted cycling ability.

dx.doi.org/10.1021/am504144d | ACS Appl. Mater. Interfaces 2014, 6, 15499−15509

CONCLUSIONS

In summary, we successfully developed a simple method to prepare size-controlled Fe_2O_3 NPs on a large scale with different morphologies, specific surface areas and pore volumes just by varying the reflux temperature and the kind of surfactant. In addition, the Fe_2O_3 NPs were further used to prepare new composite Fe_3O_4@CF_x NPs via simple carbonation of a mixture of Fe_2O_3 NPs and PVDF. This procedure could readily be extended to any metal oxide requiring functionalization with a layer of CF_x. More importantly, the composite Fe_3O_4@CF_x NPs exhibited a high reversible capacity over 900 mAh g^{-1} at a current density of 100 mA g^{-1} over 100 cycles as an anode in a LIB. Then we successfully assembled a new full cell composed of Fe_3O_4@CF_x/$LiNi_{0.5}Mn_{1.5}O_4$ with a high energy density of 371 Wh kg^{-1} (vs cathode) at the current density of 100 mA g^{-1}. This cell could cycle well over 300 cycles with 66.8% capacity retention. Noticeable, even though this cell cycled at the high temperature of 45 °C, it still exhibited a relatively high capacity of 91.6 mAh g^{-1} (vs cathode) at 100 mA g^{-1} and retained 54.6% of its reversible capacity over 50 cycles, especially with a high energy density of 316 Wh kg^{-1} (vs cathode). Moreover, this improved electrochemical performance of the Fe_3O_4@CF_x was also investigated by EIS and CV methods, from which we successfully proved that CF_x can enhance the conductivity of the electrodes and could ensure a fast Li^+ diffusion ability because the CF_x layer has a lower interfacial resistance. This new concept might be extended to revise other anode (CuO, CoO_x, MnO_x, etc.) and cathode materials ($LiMnPO_4$, $LiFePO_4$, $LiNi_{1/3}Co_{1/3}Mn_{1/3}O_2$, etc.) for advanced energy storage and conversion devices.

ASSOCIATED CONTENT

Supporting Information

Particle size distribution of Fe_2O_3 NPs synthesized under the different temperatures with using CTAB as surfactant; nitrogen adsorption−desorption isotherms and their BJH pore size distribution (inset) of Fe_2O_3 NPs prepared in the assistance of CTAB under different temperatures; XRD patterns of Fe_2O_3 NPs prepared in the assistance of different surfactants of F127, PVP and SDBS and cycling performances of Fe_3O_4, Fe_3O_4@CF_x-small, Fe_3O_4@CF_x and Fe_3O_4@CF_x-big, Fe_3O_4@C-PE, Fe_3O_4@C-SC electrodes at the current density of 200 mA g^{-1}. This material is available free of charge via the Internet at http://pubs.acs.org.

AUTHOR INFORMATION

Corresponding Authors

*J. Zheng. E-mail: jwzheng@suda.edu.cn.
*Y.-K. Sun. E-mail: yksun@hanyang.ac.kr.
*J. Ming. E-mail: mingjun6297@gmail.com.

Notes

The authors declare no competing financial interest.

ACKNOWLEDGMENTS

Financial support was received from the Nature Science Foundation of China (Nos. 20873089, 20975073), Nature Science Foundation of Jiangsu Province (No. BK2011272), Industry-Academia Cooperation Innovation Fund Projects of Jiangsu Province (No. BY2011130), Key Laboratory of Lithium Ion Battery Materials of Jiangsu Province, China Scholarship Council (File. No. 201306920005) and Graduate Research and Innovation Projects in Jiangsu Province (CXZZ13_0802). This work was also supported by a grant from the National Research Foundation of Korea (NRF) funded by the Korean government (MEST) (No. 2009-0092780) and by the Global Frontier R&D Program (No. 2013-073298) of the Center for Hybrid Interface Materials (HIM) funded by the Ministry of Science, ICT & Future Planning.

REFERENCES

(1) Poizot, P.; Laruelle, S.; Grugeon, S.; Dupont, L.; Tarascon, J. M. Nano-Sized Transition-Metaloxides as Negative-Electrode Materials for Lithium-Ion Batteries. *Nature* **2000**, *407*, 496−499.
(2) Arico, A. S.; Bruce, P.; Scrosati, B.; Tarascon, J. M.; Van Schalkwijk, W. Nanostructured Materials for Advanced Energy Conversion and Storage Devices. *Nat. Mater.* **2005**, *4*, 366−377.
(3) Taberna, L.; Mitra, S.; Poizot, P.; Simon, P.; Tarascon, J. M. High Rate Capabilities Fe_3O_4-Based Cu Nano-Architectured Electrodes for Lithium-Ion Battery Applications. *Nat. Mater.* **2006**, *5*, 567−573.
(4) Yang, J.; Takeda, Y.; Imanishi, N.; Capiglia, C.; Xie, J. Y.; Yamamoto, O. SiO_x-based Anodes for Secondary Lithium Batteries. *Solid State Ionics* **2002**, *152*, 125−129.
(5) Ren, J. G.; Wu, Q. H.; Hong, G.; Zhang, W. J.; Wu, H. M.; Amine, K.; Yang, J. B.; Lee, S. T. Silicon-Graphene Composite Anodes for High-Energy Lithium Batteries. *Energy Technol. (Weinheim, Ger.)* **2013**, *1*, 77−84.
(6) Huang, X. K.; Kim, H.; Cui, S. M.; Hurley, P. T.; Chen, J. H. Si-Composite Anode for Lithium-Ion Batteries with High Initial Coulombic Efficiency. *Energy Technol. (Weinheim, Ger.)* **2013**, *1*, 305−308.
(7) Park, M. S.; Wang, G. X.; Kang, Y. M.; Wexler, D.; Dou, S. X.; Liu, H. K. Preparation and Electrochemical Properties of SnO_2 Nanowires for Application in Lithium-Ion Batteries. *Angew. Chem., Int. Ed.* **2007**, *46*, 750−753.
(8) Xiao, H.; Xia, Y.; Zhang, W. K.; Huang, H.; Gan, Y. P.; Tao, X. Y. Template-Free Synthesis of Hollow Alpha-Fe_2O_3 Microcubes for Advanced Lithium-Ion Batteries. *J. Mater. Chem. A* **2013**, *1*, 2307−2312.
(9) Ming, J.; Ming, H.; Kwak, W. J.; Shin, C.; Sun, Y. K.; Zheng, J. The Binder Effect on Oxide-Based Anode in Lithium and Sodium-Ion Battery Applications: The Fastest Way to Ultrahigh Performance. *Chem. Commun.* **2014**, DOI: 10.1039/C4CC02657H.
(10) Lu, A. H.; Salabas, E. L.; Schuth, F. Magnetic Nanoparticles: Synthesis, Protection, Functionalization, and Application. *Angew. Chem. Int. Ed.* **2007**, *46*, 1222−1244.
(11) Gan, Y. P.; Gu, H. Q.; Xiao, H.; Xia, Y.; Tao, X. Y.; Huang, H.; Du, J.; Xu, L. S.; Zhang, W. K. Mesoporous Fe_3O_4@C Submicrospheres Evolved by a Novel Self-Corrosion Mechanism for High-Performance Lithium-Ion Batteries. *New J. Chem.* **2014**, *38* (6), 2428−2434.
(12) Ming, J.; Wu, Y.; Liang, G.; Park, J.-B.; Zhao, F.; Sun, Y.-K. Sodium Salt Effect On Hydrothermal Carbonization Of Biomass: A Catalyst for Carbon-Based Nanostructured Materials For Lithium-Ion Battery Applications. *Green Chem.* **2013**, *15*, 2722−2726.
(13) Ming, J.; Wu, Y.; Park, J.-B.; Lee, J. K.; Zhao, F.; Sun, Y.-K. Assembling Metal Oxide Nanocrystals into Dense, Hollow, Porous Nanoparticles for Lithium-Ion and Lithium−Oxygen Battery Application. *Nanoscale* **2013**, *5*, 10390.
(14) Ming, J.; Park, J. B.; Sun, Y. K. Encapsulation of Metal Oxide Nanocrystals into Porous Carbon with Ultrahigh Performances in Lithium-Ion Battery. *ACS Appl. Mater. Interfaces* **2013**, *5*, 2133−2136.
(15) Choi, S. H.; Kang, Y. C. Ultrafast Synthesis of Yolk-Shell and Cubic NiO Nanopowders and Application in Lithium Ion Batteries. *ACS Appl. Mater. Interfaces* **2014**, *6*, 2310−2314.
(16) Liu, Y.; Wang, W.; Gu, L.; Wang, Y. W.; Ying, Y. L.; Mao, Y. Y.; Sun, L. W.; Peng, X. S. Flexible CuO Nanosheets/Reduced-Graphene Oxide Composite Paper: Binder-Free Anode for High-Performance Lithium-Ion Batteries. *ACS Appl. Mater. Interfaces* **2013**, *5*, 9850−9855.

(17) Yuan, S.; Huang, X. L.; Ma, D. L.; Wang, H. G.; Meng, F. Z.; Zhang, X. B. Engraving Copper Foil to Give Large-Scale Binder-Free Porous CuO Arrays for a High-Performance Sodium-Ion Battery Anode. *Adv. Mater.* **2014**, *26*, 2273−2279.
(18) Wang, H. G.; Ma, D. L.; Huang, X. L.; Huang, Y.; Zhang, X. B. General and Controllable Synthesis Strategy of Metal Oxide/TiO2 Hierarchical Heterostructures with Improved Lithium-Ion Battery Performance. *Sci. Rep.* **2012**, *2* (701), 1−8.
(19) Ji, G.; Ding, B.; Ma, Y.; Lee, J. Y. Nanostructured SnO_2@TiO_2 Core-Shell Composites: A High-Rate Li-ion Anode Material Usable without Conductive Additives. *Energy Technol. (Weinheim, Ger.)* **2013**, *1*, 567−572.
(20) Wang, Y. L.; Xu, J. J.; Wu, H.; Xu, M.; Peng, Z.; Zheng, G. F. Hierarchical SnO_2-Fe_2O_3 Heterostructures as Lithium-Ion Battery Anodes. *J. Mater. Chem.* **2012**, *22*, 21923−21927.
(21) Marom, R.; Amalraj, S. F.; Leifer, N.; Jacob, D.; Aurbach, D. A Review of Advanced and Practical Lithium Battery Materials. *J. Mater. Chem.* **2011**, *21*, 9938−9954.
(22) Duclaux, L. Review of The Doping of Carbon Nanotubes (Multiwalled and Single-Walled). *Carbon* **2002**, *40*, 1751−1764.
(23) Ding, Z. J.; Zhao, L.; Suo, L. M.; Jiao, Y.; Meng, S.; Hu, Y. S.; Wang, Z. X.; Chen, L. Q. Towards Understanding The Effects of Carbon and Nitrogen-Doped Carbon Coating on The Electrochemical Performance of $Li_4Ti_5O_{12}$ In Lithium Ion Batteries: A Combined Experimental And Theoretical Study. *Phys. Chem. Chem. Phys.* **2011**, *13*, 15127−15133.
(24) Lei, C.; Han, F.; Li, D.; Li, W. C.; Sun, Q.; Zhang, X. Q.; Lu, A. H. Dopamine as the Coating Agent and Carbon Precursor for The Fabrication of N-Doped Carbon Coated Fe_3O_4 Composites as Superior Lithium Ion Anodes. *Nanoscale* **2013**, *5*, 1168−1175.
(25) Sun, X. J.; Zhang, Y. W.; Song, P.; Pan, J.; Zhuang, L.; Xu, W. L.; Xing, W. Fluorine-Doped Carbon Blacks: Highly Efficient Metal-Free Electrocatalysts for Oxygen Reduction Reaction. *ACS Catal.* **2013**, *3*, 1726−1729.
(26) Wu, J.; Yang, Z. R.; Li, X. W.; Sun, Q. J.; Jin, C.; Strasser, P.; Yang, R. Z. Phosphorus-Doped Porous Carbons as Efficient Electrocatalysts for Oxygen Reduction. *J. Mater. Chem. A* **2013**, *1*, 9889−9896.
(27) Boudin, F.; Andrieu, X.; Jehoulet, C.; Olsen, I. I. Microporous PVdF Gel for Lithium-ion Batteries. *J. Power. Sources* **1999**, *81*, 804−807.
(28) Ji, L. W.; Tan, Z. K.; Kuykendall, T. R.; Aloni, S.; Xun, S. D.; Lin, E.; Battaglia, V.; Zhang, Y. G. Fe_3O_4 Nanoparticle-Integrated Graphene Sheets for High-Performance Half and Full Lithium Ion Cells. *Phys. Chem. Chem. Phys.* **2011**, *13*, 7139−7146.
(29) Hariharan, S.; Ramar, V.; Joshi, S. P.; Balaya, P. Developing A Light Weight Lithium Ion Battery-An Effective Material and Electrode Design for High Performance Conversion Anodes. *RSC Adv.* **2013**, *3*, 6386−6394.
(30) Armstrong, G.; Armstrong, A. R.; Bruce, P. G.; Reale, P.; Scrosati, B. TiO_2(B) Nanowires as An Improved Anode Material for Lithium-Ion Batteries Containing $LiFePO_4$ or $LiNi_{0.5}Mn_{1.5}O_4$ Cathodes and A Polymer Electrolyte. *Adv. Mater.* **2006**, *18* (19), 2597−2600.
(31) Verrelli, R.; Hassoun, J.; Farkas, A.; Jacob, T.; Scrosati, B. A New, High Performance CuO/$LiNi_{0.5}Mn_{1.5}O_4$ Lithium-Ion Battery. *J. Mater. Chem. A* **2013**, *1*, 15329−15333.
(32) Xu, G. L.; Xu, Y. F.; Fang, J. C.; Fu, F.; Sun, H.; Huang, L.; Yang, S. H.; Sun, S. G. Facile Synthesis of Hierarchical Micro/Nanostructured MnO Material and Its Excellent Lithium Storage Property and High Performance as Anode in a MnO/$LiNi_{0.5}Mn_{1.5}O_4$ Lithium Ion Battery. *ACS Appl. Mater. Interfaces* **2013**, *5*, 6316−6323.
(33) Ming, J.; Kwak, W. J.; Youn, S. J.; Ming, H.; Hassoun, J.; Sun, Y. K. Lithiation of an Iron Oxide-based Anode for Stable, High-Capacity Lithium-Ion Batteries of Porous Carbon-Fe_3O_4/$Li[Ni_{0.59}Co_{0.16}Mn_{0.25}]O_2$. *Energy Technol. (Weinheim, Ger.)* **2014**, DOI: 10.1002/ente.201402031.
(34) Ming, H.; Ma, Z.; Huang, H.; Lian, S. Y.; Li, H. T.; He, X. D.; Yu, H.; Pan, K. M.; Liu, Y.; Kang, Z. H. Nanoporous TiO_2 Spheres with Narrow Pore Size Distribution and Improved Visible Light Photocatalytic Abilities. *Chem. Commun.* **2011**, *47*, 8025−8027.
(35) Ming, J.; Wu, Y.; Wang, L.; Yu, Y.; Zhao, F. CO_2-assisted Template Synthesis of Porous Hollow Bi-phase γ-/α-Fe_2O_3 Nanoparticles with High Sensor Property. *J. Mater. Chem.* **2011**, *21*, 17776−17782.
(36) Roth, E. P.; Doughty, D. H.; Franklin, J. DSC Investigation of Exothermic Reactions Occurring at Elevated Temperatures in Lithium-Ion Anodes Containing PVDF-based binders. *J. Power Sources* **2004**, *134*, 222−234.
(37) Hochart, F.; Levalois-Mitjaville, J.; Jaeger, R. D.; Gengembre, L.; Grimblot, J. Plasma Surface Treatment of Poly(acrylonitrile) Films by Fluorocarbon Compounds. *Appl. Surf. Sci.* **1999**, *142*, 574−578.
(38) Yang, S.; Liu, H. R.; Zhang, Z. C. Design and Fabrication of Hollow, Magnetic and Fluorescent CdS-Magnetite-Poly(styrene-co-methyl methacrylate) Microspheres. *New J. Chem.* **2009**, *33*, 620−625.
(39) Jeong, S.-J.; Xia, G. D.; Kim, B. H.; Shin, D. O.; Kwon, S.-H.; Kang, S.-W.; Kim, S. O. Universal Block Copolymer Lithography for Metals, Semiconductors, Ceramics, and Polymers. *Adv. Mater.* **2008**, *20*, 1898−1904.
(40) Langan, J. G.; Shorter, J. A.; Xin, X.; Joyce, S. A.; Steinfeld, J. I. Reactions of Laser-generated CF_2 on Silicon and Silicon Oxide Surfaces. *Surf. Sci.* **1989**, *207*, 344−353.
(41) Minami, I.; Inada, T.; Sasaki, R.; Nanao, H. Tribo-chemistry of Phosphonium-derived Ionic Liquids. *Tribol. Lett.* **2010**, *40*, 225−235.
(42) Cai, Y. F.; Pan, Y. G.; Xue, J. Y.; Sun, Q. F.; Su, G. Z.; Li, X. Comparative XPS Study between Experimentally and Naturally Weathered Pyrites. *Appl. Surf. Sci.* **2009**, *255*, 8750−8760.
(43) Liu, L.; Zhou, M.; Yi, L. H.; Guo, H. P.; Tan, J. L.; Shu, H. B.; Yang, X. K.; Yang, Z. H.; Wang, X. Y. Excellent Cycle Performance of Co-Doped FeF_3/C Nanocomposite Cathode Material for Lithium-ion Batteries. *J. Mater. Chem.* **2012**, *22*, 17539−17550.
(44) Ma, D. L.; Cao, Z. Y.; Wang, H. G.; Huang, X. L.; Wang, L. M.; Zhang, X. B. Three-Dimensionally Ordered Macroporous FeF_3 and Its in Situ Homogenous Polymerization Coating for High Energy and Power Density Lithium Ion Batteries. *Energy Environ. Sci.* **2012**, *5* (9), 8538−8542.
(45) Wang, J. Z.; Zhong, C.; Wexler, D.; Idris, N. H.; Wang, Z. X.; Chen, L. Q.; Liu, H. K. Graphene-encapsulated Fe_3O_4 Nanoparticles with 3D Laminated Structure as Superior Anode in Lithium Ion Batteries. *Chem.—Eur. J.* **2011**, *17*, 661−667.
(46) Xie, J.; Tanaka, T.; Imanishi, N.; Matsumura, T.; Hirano, A.; Takeda, Y.; Yamamoto, O. Li-ion Transport Kinetics in $LiMn_2O_4$ Thin Films Prepared by Radio Frequency Magnetron Sputtering. *J. Power Sources* **2008**, *180*, 576−581.
(47) Ming, J.; Kwak, W.-J.; Park, J.-B.; Shin, C.-D.; Lu, J.; Curtiss, L.; Amine, K.; Sun, Y.-K. A Physical Pulverization Strategy for Preparing a Highly Active Composite of CoOx and Crushed Graphite for Lithium-Oxygen Batteries. *ChemPhysChem* **2014**, *15*, 2070−2076.
(48) Chen, Y.; Xi, H.; Lu, L.; Xue, J. M. Synthesis of Porous Hollow Fe_3O_4 Beads and Their Applications in Lithium Ion Batteries. *J. Mater. Chem.* **2012**, *22*, 5006−5012.
(49) Zhang, W. M.; Wu, X. L.; Hu, J. S.; Guo, Y. G.; Wan, L. J. Carbon Coated Fe_3O_4 Nanospindles as a Superior Anode Material for Lithium-Ion Batteries. *Adv. Funct. Mater.* **2008**, *18*, 3941−3946.
(50) Zhou, G. M.; Wang, D. W.; Li, F.; Zhang, L. L.; Li, N.; Wu, Z. S.; Wen, L.; Lu, G. Q.; Cheng, H. M. Graphene-wrapped Fe_3O_4 Anode Material with Improved Reversible Capacity and Cyclic Stability for Lithium Ion Batteries. *Chem. Mater.* **2010**, *22*, 5306−5313.
(51) Ming, H.; Ming, J.; Li, X. W.; Zhou, Q.; Jin, L. L.; Fu, Y.; Adkins, J.; Kang, Z. H.; Zheng, J. W. Synthesis of N-Doped Carbon Coated Metal Oxide Nanoparticles for Enhanced Li-Ion Storage Ability. *RSC Adv.* **2013**, *3*, 15613−15617.
(52) Oh, S. W.; Myung, S.-T.; Kang, H. B.; Sun, Y.-K. Effects of Co Doping on $Li[Ni_{0.5}Co_xMn_{1.5-x}]O_4$ Spinel Materials for 5V Lithium Secondary Batteries via Co-Precipitation. *J. Power Sources* **2009**, *189*, 752−756.
(53) Arbizzani, C.; Giorgio, F. D.; Porcarelli, L.; Mastragostino, M.; Khomenko, V.; Barsukov, V.; Bresser, D.; Passerini, S. Use of Non-

conventional Electrolyte Salt and Additives in High-Voltage Graphite/$LiNi_{0.4}Mn_{1.6}O_4$ Batteries. *J. Power Sources* **2013**, *238*, 17−20.